



Cite this: *Nanoscale*, 2018, **10**, 3969

Atomistic and continuum scale modeling of functionalized graphyne membranes for water desalination†

Muralikrishna Raju, ^a Pavan B. Govindaraju,^a Adri C. T. van Duin^b and Matthias Ihme ^{*a}

Recent theoretical and experimental studies reported ultra-high water permeability and salt rejection in nanoporous single-layer graphene. However, creating and controlling the size and distribution of nanometer-scale pores pose significant challenges to application of these membranes for water desalination. Graphyne and hydrogenated graphyne have tremendous potential as ultra-permeable membranes for desalination and wastewater reclamation due to their uniform pore-distribution, atomic thickness and mechano-chemical stability. Using molecular dynamics (MD) simulations and upscale continuum analysis, the desalination performance of bare and hydrogenated α -graphyne and γ -(2,3,4)-graphyne membranes is evaluated as a function of pore size, pore geometry, chemical functionalization and applied pressure. MD simulations show that pores ranging from 20 to 50 Å² reject in excess of 90% of the ions for pressures up to 1 GPa. Water permeability is found to range up to 85 L cm⁻² day⁻¹ MPa⁻¹, which is up to three orders of magnitude larger than commercial seawater reverse osmosis (RO) membranes and up to ten times that of nanoporous graphene. Pore chemistry, functionalization and geometry are shown to play a critical role in modulating the water flux, and these observations are explained by water velocity, density, and energy barriers in the pores. The atomistic scale investigations are complemented by upscale continuum analysis to examine the performance of these membranes in application to cross-flow RO systems. This upscale analysis, however, shows that the significant increase in permeability, observed from MD simulations, does not fully translate to current RO systems due to transport limitations. Nevertheless, upscale calculations predict that the higher permeability of graphyne membranes would allow up to six times higher permeate recovery or up to 6% less energy consumption as compared to thin-film composite membranes at currently accessible operating conditions. Significantly higher energy savings and permeate recovery can be achieved if higher feed-flow rates can be realized.

Received 26th October 2017,
Accepted 31st January 2018

DOI: 10.1039/c7nr07963j

rsc.li/nanoscale

1. Introduction

The scarcity of fresh water represents a serious global challenge, which is predicted to worsen in the future owing to population growth, increased industrialization and growing energy needs. Although water covers 75% of the Earth's surface, more than 97% is contained in the form of salty water in oceans and seas. Desalination is a promising approach to produce fresh water. However, currently this technology only accounts for less than one percent of the world's fresh water

supply.^{1–3} Commercial desalination technologies, including reverse osmosis (RO) and thermal desalination face two major challenges, namely high capital costs and low energy efficiency. Currently, RO is the most energy-efficient desalination technique^{4,5} at levels of 1.8–5.7 kWh m⁻³. In contrast, thermal desalination methods such as multi-stage flash and multi-effect distillation are more energy intensive by an order of magnitude.^{4,6,7}

Recently, nanoporous membranes have attracted considerable attention due to their remarkable potential for water desalination.⁸ Salt ions possess a larger effective volume in solution compared to water molecules owing to their hydration shell. Thus, ions can be rejected by nanopores with smaller diameters, while allowing fast convective water flow. Several nanoscale materials including metal-organic frameworks (MOFs), zeolites,^{9,10} and carbon nanotubes (CNTs)^{11–13} have been extensively studied for both water permeability and desalina-

^aDepartment of Mechanical Engineering, Stanford University, Stanford, CA 94305, USA. E-mail: mihme@stanford.edu

^bDepartment of Mechanical and Nuclear Engineering, The Pennsylvania State University, University Park, PA 16802, USA

†Electronic supplementary information (ESI) available: Model description and parameters for upscale analysis. See DOI: 10.1039/C7NR07963J

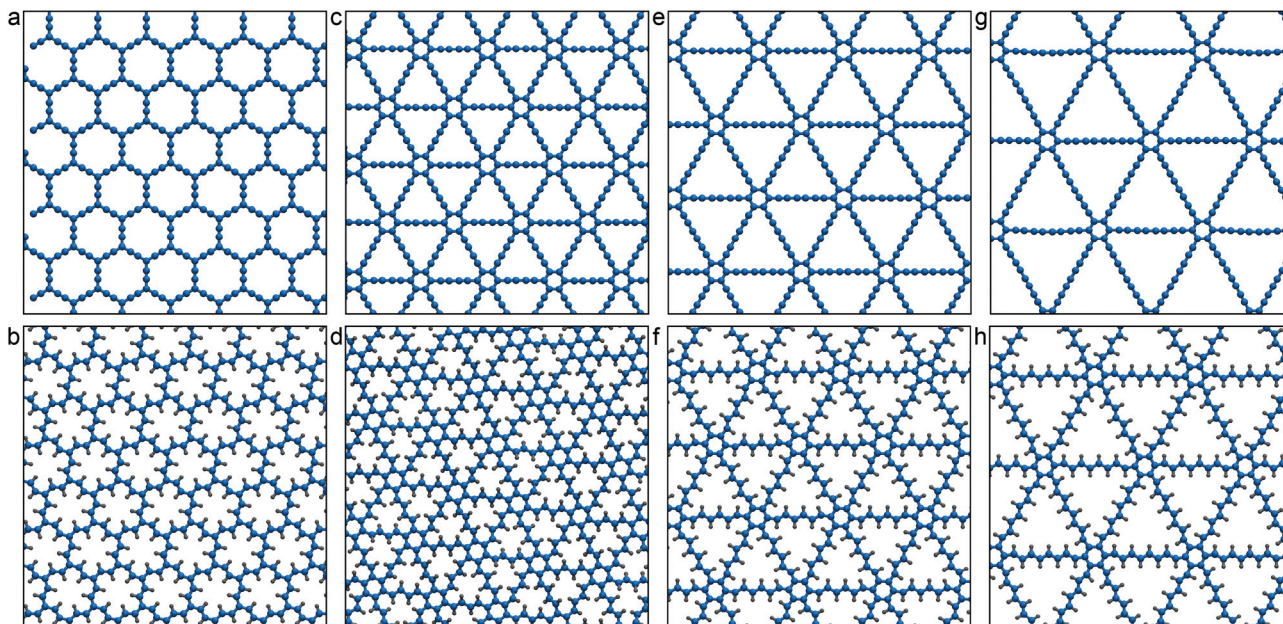


Fig. 1 Graphyne membranes: (a) α -graphyne ($7.01 \text{ \AA} \times 6.07 \text{ \AA}$), (b) hydrogenated α -graphyne ($7.01 \text{ \AA} \times 6.07 \text{ \AA}$), (c) γ -2-graphyne (9.65 \AA mes 8.35 \AA), (d) hydrogenated γ -2-graphyne ($9.07 \text{ \AA} \times 7.88 \text{ \AA}$), (e) γ -3-graphyne ($12.28 \text{ \AA} \times 10.64 \text{ \AA}$), (f) hydrogenated γ -3-graphyne ($12.13 \text{ \AA} \times 10.51 \text{ \AA}$), (g) γ -4-graphyne ($14.92 \text{ \AA} \times 12.92 \text{ \AA}$), and (h) hydrogenated γ -4-graphyne ($14.51 \text{ \AA} \times 12.66 \text{ \AA}$) employed in this study. The unit cell dimensions are included in parentheses.

tion. These materials, however, have their disadvantages. Zeolites and MOFs have low water flux due to their complex pore architecture,^{9,10} while CNTs, despite allowing for faster water permeation, exhibit low salt ion rejection along with the challenge of producing large-scale high-performance CNT arrays.^{11–13} Recently single-layer graphene and MoS₂ membranes that contain artificial nanopores have been proposed for nanofiltration.^{6,14–16} However, producing membranes with such extremely narrow pores at well controlled pore densities is a considerable technological challenge. This is crucial since the pore area critically dictates both the water flux and salt rejection ability of nanoporous membranes, and pore areas less than 40 to 60 Å² are essential for achieving significant (>80%) salt rejection.^{6,16} Also critical to desalination performance are the geometry and chemical functionalization of the pore. Specifically, pore functionalization not only modifies the accessible pore area but also dictates whether the pore is hydrophilic or hydrophobic, which has been shown to determine the water flux and salt rejection ability of the membrane.^{6,16} Membranes possessing regular pore distribution with controllable pore diameter are therefore of considerable interest.

Graphyne membranes,^{17–24} unlike graphene, provide uniform and controllable pore-size distribution with high membrane porosity. Graphyne is a family of 2D carbon allotropes, composed of both sp- and sp²-hybridized carbons, involving different conjugations between acetylene and phenyl groups.^{17–21,25} The different configurations are built by the insertion of acetylene (–C≡C–) units into graphene by formal carbo-merization. The atomic structures of two highly sym-

metric configurations of bare and hydrogenated α - and γ -graphyne are shown in Fig. 1. The structure of α -graphyne (Fig. 1a) is actually the total carbo-mer of graphene and can be viewed as an assembly of fused carbo-benzene rings exhibiting hexagonal pores. In comparison, γ -graphyne (Fig. 1c, e and g) arises from partial carbo-merization of graphene and can be viewed as an assembly of phenyl rings connected by acetylene chains exhibiting triangular pores. The pore size of γ -graphyne can be adjusted by changing the number of acetylene bonds, n , that connect the adjacent phenyl rings. The different configurations of γ -graphyne are referred to as γ - n -graphyne hereafter. γ -1-graphyne (or graphyne) and γ -2-graphyne (or graphdiyne) have been successfully synthesized in large quantities.^{7,18,19} Graphyne membranes exhibit interesting mechanical, chemical and electronic properties due to their unique topology. In particular, they exhibit directionally dependent Diraccones, high electron mobility,^{26,27} and have Young's modulus in excess of 350 GPa.^{28,29}

Previous MD studies^{7,30} have evaluated the potential of bare γ -graphyne membranes for desalination. However, in desalination systems, bare graphyne membranes will get functionalized in the presence of protons or hydroxyl radicals in water.³¹ Therefore, the consideration of functionalization is essential to realistically evaluate their potential for seawater desalination. To this end, we determine the desalination performance of bare and hydrogenated (H) α - and γ - n -graphyne membranes with $n = \{2, 3, 4\}$. These structures are shown in Fig. 1b, d, f and g. In addition, hydrogenation can be expected to improve the chemical stability of graphyne membranes by the saturation of in-plane p-orbitals, promoted by covalent bonding

with hydrogen. For instance, DFT calculations by Longuinhos *et al.*³² report suppressed chemical frustration of the planar lattice in hydrogenated α -graphyne as compared to pristine α -graphyne due to passivation of in-plane p-orbitals, thus inhibiting the formation of the destabilizing π -bonds from these orbitals. In addition, previous MD studies^{7,30,33–35} fixed the position of the carbon atoms in the graphyne membranes to their initial lattice positions to prevent out of plane displacement. This is not directly representative of realistic desalination systems, and as discussed later, frozen graphyne membranes exhibit appreciably lower water permeability and higher salt rejection than flexible graphyne membranes. The effect of the modeling methodology on permeability and salt rejection requires consideration in evaluating the desalination performance of nanoporous membranes.

The objective of this study is to examine, through MD simulations and up-scaling analysis, the performance of single-layer graphyne and hydrogenated graphyne membranes in effectively separating salt ions from water for use in desalination systems. The water permeability and salt rejection obtained from MD simulations are subsequently employed in an upscale analysis to quantify improvements in performance and energy cost of a cross-flow RO plant. In the remaining sections, we discuss effects of applied hydrostatic pressure, pore size, chemistry, and geometry on water flux and salt rejection capability of the membranes and present results from the upscale analysis of the membranes to evaluate the potential of nanoporous graphyne for water purification.

2. Computational methods

In this study, MD simulations were carried out to predict the desalination performance of bare and hydrogenated graphyne membranes. The computational setup is illustrated in Fig. 2. A typical computational box consists of a single-layer graphyne or hydrogenated graphyne, a graphene sheet (used as a rigid piston to apply the external pressure), salt ions and water. The saline water was placed between the graphene and graphyne sheet and pure water was added on the other side of the graphyne sheet. In our simulations, we used periodic graphyne sheets with (9×9) unit cells in the spanwise x - y plane, the saline water box measuring 40 Å in the z -direction and the pure water box measuring 5 Å in the z -direction. The salt water in our system corresponds to a water density of 1 g cm⁻³ and salt concentration of 1.0 M, which is higher than the normal salinity of seawater (0.6 M). This higher salinity was chosen to increase the occurrence of ion-pore interactions and to obtain better statistics for a given system size in the time-scale of our MD simulations.

We consider bare and hydrogenated α -graphyne and γ - n -graphyne with $n = \{2, 3, 4\}$ membranes to study effects of pore size, pore geometry and pore chemistry on the rate of water permeation and ion rejection. Table 1 shows the accessible pore area for bare and hydrogenated α -graphyne and γ - n -graphyne membranes.

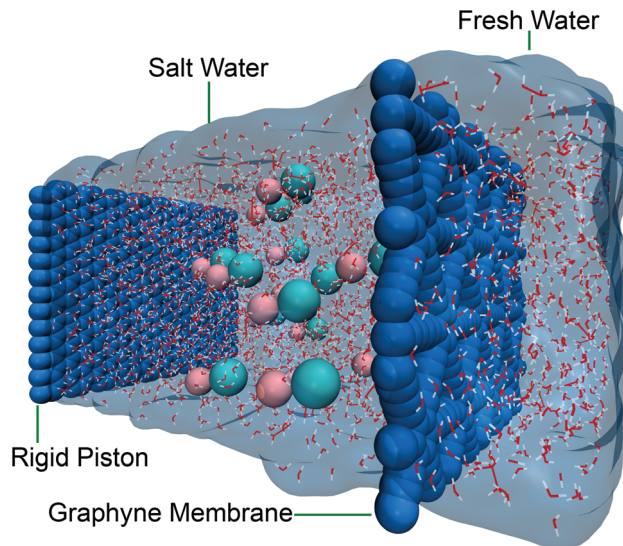


Fig. 2 Desalination simulation setup. Schematic of the simulation box consisting of a desalination membrane – graphyne sheet (blue), water (transparent blue), ions (green and pink) and a graphene sheet (blue).

MD simulations are performed using the first-principles-based ReaxFF reactive force-field method,³⁶ which can simulate chemical reactions with significantly higher efficiencies than *ab initio* MD calculations while still retaining near-quantum mechanical accuracy. ReaxFF is a bond-order based force-field method with a polarizable charge model, which enables the method to model the breaking and formation of bonds and the associated charge rearrangements during an energy-conserving MD simulation. The ReaxFF force field method can therefore account for water polarizability and water ionization arising in saline aqueous solutions as well as the mechanical and chemical properties of graphyne membranes. The ReaxFF force field has been employed to investigate mechanical properties of graphyne as reported in Cranford *et al.*^{25,28} Here, the water-graphyne interactions were modeled using the C/O/H ReaxFF force field parameters employed in Hatzell *et al.*³⁷ and the water molecules were modeled using the same O/H ReaxFF parameters as employed in previous ReaxFF descriptions.^{37–39} The C/H/O/K/Cl force field development is described in detail in Rahaman *et al.*^{40,41} The ReaxFF reactive force field method has been shown to provide an accurate account of the chemical and mechanical

Table 1 Accessible pore area and formation energy. The accessible pore area for bare and hydrogenated α -graphyne and γ - $\{2, 3, 4\}$ -graphyne membranes and the formation energy of hydrogenated graphyne membranes

Membrane	Bare (Å ²)	Hydrogen (Å ²)	E_f (eV per H ₂)
α -Graphyne	29.91	20.48	-1.81
γ -2-Graphyne	25.15	15.72	-1.77
γ -3-Graphyne	45.57	35.31	-1.55
γ -4-Graphyne	71.89	59.90	-1.54

behavior of hydrocarbons,³⁶ graphene,⁴² graphyne,^{25,28} carbon nanotubes^{43,44} and other carbon nanostructures.^{39,45}

All simulations were performed using the LAMMPS package.⁴⁶ For each simulation, the system was first energy minimized for 10 000 steps. Subsequently, the system was equilibrated in the canonical *NPT* (constant number of atoms (*N*), constant pressure (*P*) and constant temperature (*T*)) ensemble for 250 ps at a pressure of 1 atm and temperature of 313 K. The temperature was chosen to match the experimental temperature in Surwade *et al.*¹⁵ Simulations were performed with a time step of 0.10 fs using the Nose–Hoover thermostat with a coupling time constant of 10 fs and Nose–Hoover barostat with a coupling constant of 100 fs to control the temperature and pressure of the entire system, respectively. Subsequently, the production non-equilibrium MD simulations were run in the *NVT* ensemble (constant number of atoms, constant volume (*V*) and constant temperature) for another 250 ps at 313 K where different external pressures (100–2500 MPa) were applied on the rigid graphene sheet to examine the water desalination through the graphyne membranes. The atom trajectories were collected every 10 fs to analyze the results.

In experimental systems, desalination membranes are flexible and to account for this, the membrane atoms are allowed to move during the MD simulations. To simulate the effect of a substrate that would prevent the entire membrane from moving out of plane, we tethered five carbon atoms (<2%) in the membrane to their original position. These atoms were randomly chosen from the corners of the acetylene chains of the graphyne membrane to not affect the flexibility of the chains.

In functionalized membranes, it is important to account for the flexibility of the membrane, since the functionalizations (here H-) can bend out of plane and increase the effective accessible pore area. The ReaxFF reactive force-field method enables simulations of flexible membranes to incorporate the effect of membrane deformation on water permeation and salt rejection. This also allows investigating the stability of graphyne membranes in saline environments at different applied pressures.

To further validate the ReaxFF force field, we computed the formation energy of graphyne membranes as:

$$E_f = E_{\text{H+gra}} - E_{\text{gra}} - mE_{(\text{H}_2)}, \quad (1)$$

where $E_{\text{H+gra}}$ is the energy of hydrogenated graphyne, E_{gra} is the energy of bare graphyne, $E_{(\text{H}_2)}$ is the energy of a hydrogen molecule and m is twice the number of hydrogen atoms in the corresponding hydrogenated graphyne. Results for hydrogenated graphyne membranes are reported in Table 1. The formation energy of hydrogenated γ -2-graphyne membranes predicted with the ReaxFF force field (−1.77 eV per H_2) is in good agreement with DFT calculations of Psofogiannakis *et al.*³¹ (−1.81 eV per H_2). We further validate the force field by computing the self-diffusivity of bulk water. The self-diffusion coefficient of water at 298 K given by ReaxFF ($2.1 \times 10^{-5} \text{ cm}^2 \text{ s}^{-1}$)

is in good agreement with values given by diaphragm-cell technique⁴⁷ ($2.272 \times 10^{-5} \text{ cm}^2 \text{ s}^{-1}$) and pulsed magnetic field gradient nuclear magnetic resonance ($2.299 \times 10^{-5} \text{ cm}^2 \text{ s}^{-1}$) studies.⁴⁸

Free energy barriers for water molecule passing across the membranes were calculated along the reaction coordinate (z) using umbrella sampling simulations.⁴⁹ These simulations were performed using version 1.3 of PLUMED⁵⁰ called from within the LAMMPS package.⁴⁶ The width of each umbrella window is 0.25 Å. A biasing potential of $25 \text{ kcal mol}^{-1} \text{ \AA}^{-2}$ was applied on the z -coordinate of the water oxygen in each window. All simulations were conducted for 500 ps, with the last 400 ps for data analysis. The yielded umbrella histograms were then unbiased and combined using the weighted histogram analysis method⁵¹ to obtain the free energy profile.

3. Results

3.1. Atomistic-scale analysis

Water fluxes. Computed water fluxes as a function of the applied external pressure through bare graphyne membranes are shown in Fig. 3a and those for hydrogenated graphyne membranes are shown in Fig. 3b. These results indicate that the water flux through the membranes decreases in the following order: γ -4-graphyne, H γ -4-graphyne, γ -3-graphyne, α -graphyne, γ -2-graphyne, H γ -3-graphyne, H α -graphyne and H γ -2-graphyne. The water flow rate increases with applied pressure and accessible pore area. The hydrogenated γ -2-graphyne membrane has the lowest pore size and does not allow water to pass through for pressures lower than 100 MPa. Larger pores allow for water to flow at a constant rate, which is proportional to the external pressure. Pore functionalization significantly reduces the water flux, ranging from ~50% for γ -4-graphyne to ~92% for γ -2-graphyne at 2500 MPa and hence is an important effect to be considered while evaluating membranes for desalination. It is interesting to note that the hexagonal pores in α -graphyne with $A = 29.91 \text{ \AA}^2$ have a higher water permeability than the triangular pore ($A = 32.81 \text{ \AA}^2$) in H γ -3-graphyne. This indicates that not only pore functionalization but also pore geometry critically affects the rate of water permeation. As discussed later, we show that hexagonal pores have a higher water permeability per unit area as compared to triangular pores.

Salt rejection. In addition to water permeability, the other equally important aspect of water desalination systems is the ability of the membrane to reject ions. The percentage of ions rejected by the bare graphyne membranes as a function of applied external pressure is shown in Fig. 3c and by the hydrogenated graphyne membranes is shown in Fig. 3d. Salt rejection is calculated from the salinity of the permeate solution relative to the salinity of the feed solution after half of the water molecules from the feed side have passed to the permeate side. Our results indicate that, excluding γ -4-graphyne, all membranes achieve salt rejections in excess of 75%, for pressures up to 2 GPa. This indicates that for open pore areas up to

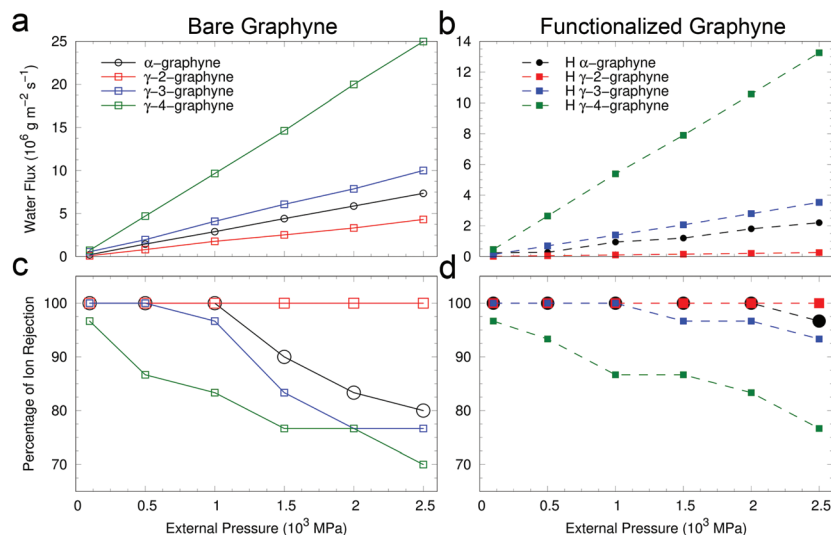


Fig. 3 Water flux and salt rejection. Water flux as a function of applied pressure for (a) bare graphyne and (b) hydrogenated graphyne membranes. Percentage of ion rejection as a function of applied pressure for (c) bare graphyne and (d) hydrogenated graphyne membranes.

~ 50 Å² the membrane rejects the majority of the salt ions. γ -{2,3}-graphyne, H γ -3-graphyne, α -graphyne and H α -graphyne membranes allow for high water fluxes while still rejecting more than 90% of the ions for pressures up to 1 GPa, and are therefore the best candidates for desalination among the various membranes considered in our study.

Salt rejection decreases with increasing pore size and applied pressure. While this behavior is expected from an available pore area argument, the decrease with applied pressure is noteworthy. This can be explained by the fact that the ions in solution have a larger effective volume owing to their hydration shell. The hydration diameter $d_{\text{ion-H}}$ of Na⁺ is 6.3 Å and Cl⁻ is 7.1 Å as compared to the ~ 2.8 Å van der Waals diameter of water molecules. This larger volume makes ions more responsive to rising pressure than water molecules. The associated increase in ion flux with applied mechanical pressure is opposite to the behavior observed in RO membranes.⁵² Specifically, in diffusive RO membranes, the driving force for ion flux is osmotic pressure and water flux increases faster with feed pressure than the corresponding ion flux. As feed pressure is increased, the salt passage is increasingly overcome as water is pushed through the RO membrane at a faster rate than salt can be transported, thus resulting in lower permeate salinity. Previous studies on nanoporous graphene,⁶ MoS₂¹⁶ and bare γ -graphyne³⁰ membranes observe a similar increase in ion flux with applied pressure.

Pore chemistry is also found to affect salt rejection. Hydrogenated membranes exhibit an improved salt rejection performance as compared to bare membranes because of their lower pore area. However, the improved salt rejection comes at the expense of lower water flux through the membrane. Hydrogenated nanoporous graphene membranes were reported⁶ to exhibit improved salt rejection as compared to hydroxylated graphene membranes owing to their hydrophobic nature.

We find that simulating the desalination membrane as a rigid or flexible membrane affects the salt rejection. To quantify this effect, we perform a desalination MD simulation with γ -3-graphyne membrane while keeping the membrane atoms frozen to their initial position with a driving pressure of 1500 MPa. By fixing the position of the atoms in the membrane, γ -3 membranes show 94% salt rejection. Whereas on allowing the membranes to be flexible as shown in Fig. 3, the salt rejection reduces to 86% at 1500 MPa. This can be explained by the increased pore area, which was found to vary by up to 8.1% for γ -3-graphyne membranes at this specific operating pressure. The effect on water flux is less pronounced and we observe that fixing the membrane position reduces the water flux by 4.2% as compared to the flexible membrane. Flexible membranes thus have a higher water and ion flux as compared to rigid membranes and hence lower salt rejection performance. Previous MD desalination studies have employed rigid membranes and this effect on salt rejection has to be considered when interpreting results.

Regarding the practical application of graphyne membranes to water desalination, apart from high water permeability and salt rejection, graphyne membranes require mechanical and chemical stability. Mechanically, graphyne membranes have Young's modulus larger than 350 GPa.^{28,29} We observe from our simulations that graphyne membranes are stable up to applied hydrostatic pressures of 3.5 GPa. The membranes with smaller pores, γ -2-graphyne and H γ -2-graphyne, are more susceptible to fracture than membranes with larger pores. However, these pressures are far greater than typical operating pressures of RO plants (<200 bar) and confirm robustness of graphyne membranes for RO desalination. The cleavage is initiated at the center of the acetylene chains at the C–C single bond connecting the acetylene (–C≡C–) units.

Membrane performance. The slope of water flux vs. pressure as shown in Fig. 3a and b gives the water permeability for the

membranes. The water permeability ranges from 10^3 to 10^4 $\text{g m}^{-2} \text{s}^{-1} \text{MPa}^{-1}$ for the graphyne and hydrogenated graphyne membranes considered in our study. Previous MD studies^{30,33} on bare γ -3-graphyne membranes report permeabilities of the order of 10^4 $\text{g m}^{-2} \text{s}^{-1} \text{MPa}^{-1}$ and are comparable to the permeabilities reported in this study. MD studies by Zhu *et al.*⁷ reported permeabilities that are lower by an order of magnitude through γ -3-graphyne membranes. These differences can be attributed to the different potentials employed in the MD simulations. Osmotic pressure gradient experiments¹⁵ through nanoporous graphene report water permeability up to 7×10^2 $\text{g m}^{-2} \text{s}^{-1} \text{MPa}^{-1}$, which is approximately an order of magnitude lower than the permeability observed in graphyne membranes in this study. This difference can be explained by the lower porosity in nanoporous graphene membranes.

Water permeability and ion rejection are the two important factors determining the effectiveness and performance of water desalination membranes. In Fig. 4, the water permeability and ion rejection of graphyne membranes is compared with the performance of MFI-type zeolite,⁹ brackish RO,⁵³ nanofiltration RO,⁵³ TFC RO,⁵⁴ high-flux RO,⁵³ commercial seawater RO,⁵³ nanoporous graphene¹⁶ and MoS_2 membranes.¹⁶ As shown in Fig. 4, the permeation rate of graphyne membranes is up to three orders of magnitude larger than seawater RO membranes ($\times 3305$ for γ -4-graphyne) and up to ten times larger than nanoporous graphene and MoS_2 membranes. Graphyne membranes inherently have a uniform pore distribution, higher porosity, and controllable pore geometry than nanoporous graphene and MoS_2 membranes. Graphyne and hydrogenated graphyne are thus potentially superior and efficient membranes for water desalination.

Functionalization and pore geometry. The ordering and structure of water molecules as they pass through the pores

directly affect the water flux and salt rejection rates of the membranes. The water structure in the pore vicinity is in turn determined by the pore geometry as well as pore functionalization. To investigate the structure and water–membrane interaction as the water passes through the membrane, we compute the probability density of hydrogen and oxygen atoms of water molecules in the pore vicinity; these results are shown in Fig. 5. To obtain these density plots, we first segment the simulation cell within 1 \AA of the pore on both the feed and permeate side to a mesh of cubic boxes with dimensions $(0.30 \times 0.30 \times 0.30 \text{ \AA}^3)$. We then counted the number of times a particular atom type (*i.e.*, oxygen and hydrogen) is located in each of the grids over the entire duration of the simulation. These results are normalized by the highest count recorded in any of the grids. We can observe that the pore geometry determines the way water molecules flow through the membrane. For hexagonal pores, the water passes through the membrane with an approximately circular cross-section, with the oxygen atoms passing through the center of the pore. For bare or hydrogenated triangular pores, the water passes through the membrane with a triangular cross-section *via* multiple, distinct channels. As shown in Fig. 5 we can observe three distinct water channels through bare and H γ -3-graphyne membranes. Hydrogenated graphyne membranes are hydrophobic like the bare membranes and irrespective of the pore functionalization the oxygen atoms pass towards the center of the pore, while hydrogen atoms pass closer to the C-atoms in the membrane. This behavior is also observed in hydrogenated graphene nanopores.⁶

To understand the reason for these distinct water channels, we compute the free energy surface (FES) of the water mole-

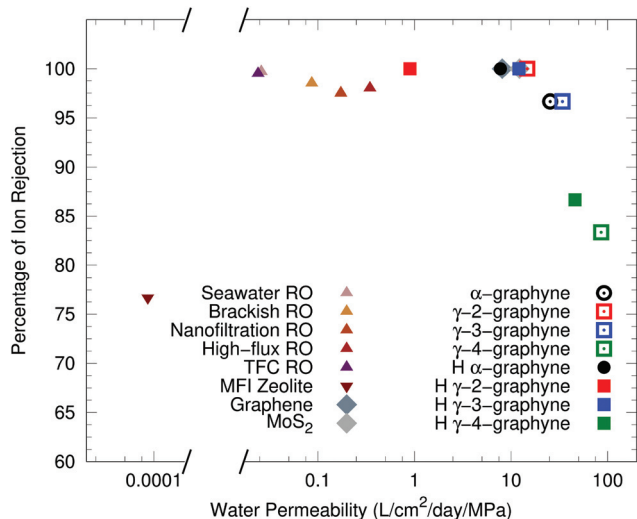


Fig. 4 Performance of graphyne membranes. Performance of various membranes in terms of their ion rejection and water permeation rate. Water permeation rate is expressed per unit area of the membrane and per unit pressure as $\text{L cm}^{-2} \text{day}^{-1} \text{MPa}^{-1}$.

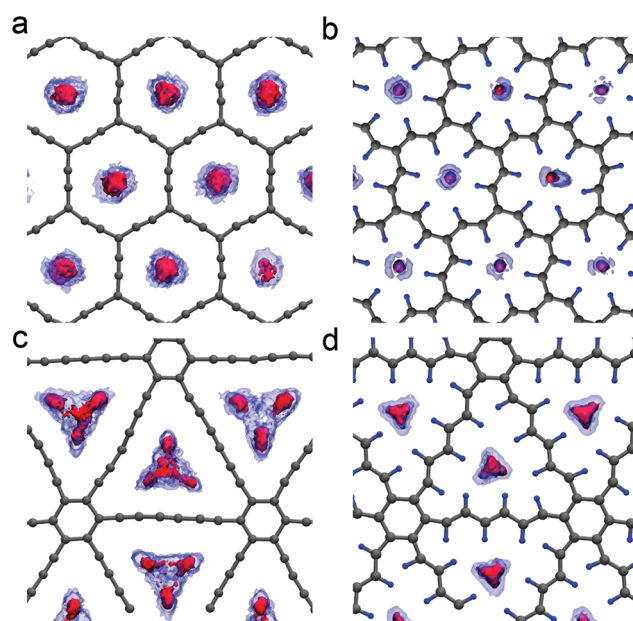


Fig. 5 Effect of pore functionalization on water permeation and salt rejection. Probability density maps of oxygen (red) and hydrogen (blue) inside (a) α -graphyne, (b) hydrogenated α -graphyne, (c) γ -3-graphyne and (d) hydrogenated γ -3-graphyne.

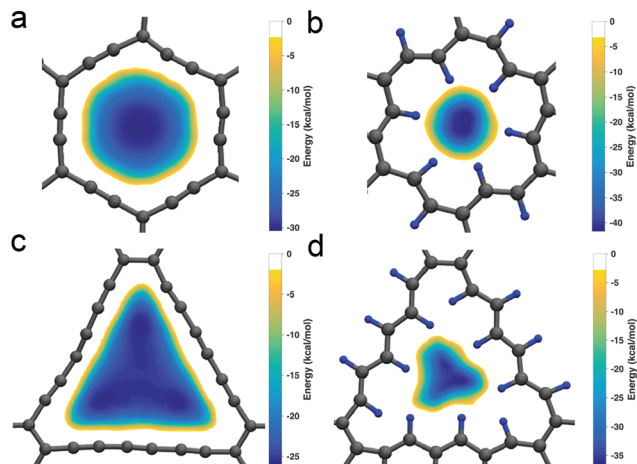


Fig. 6 Free energy surfaces. Free energy of a water molecule inside a nanopore of (a) α -graphyne, (b) hydrogenated α -graphyne, (c) γ -3-graphyne and (d) hydrogenated γ -3-graphyne; computed using metadynamics simulations.

cules in the nanopores of the graphyne membranes using a well-tempered metadynamics simulation.⁵⁰ The collective variables are the x - and y -coordinates of water oxygen over the graphyne x - y plane. We use a hill height of $0.1 \text{ kcal mol}^{-1}$ and a width of 0.10 \AA , and hills are added at every 100 timesteps. FESs are reconstructed from the Gaussian bias potentials added during the metadynamics trajectory. Results from these computations are presented in Fig. 6. The FES of water molecule in the α -graphyne and hydrogenated α -graphyne nanopore have a circular cross-section, while the FES of γ -3-graphyne and hydrogenated γ -3-graphyne have a triangular cross-section, as also observed in the oxygen density plots in Fig. 5. The minimum energy of the FES in the γ -3-graphyne has three distinct spots, which can be visualized as the vertices of a triangle, giving rise to three distinct water channels.

Fig. 7a and b shows the free energy barriers for a water molecule moving across the pore of the bare and hydrogenated graphyne membranes. We can observe that the trends in the

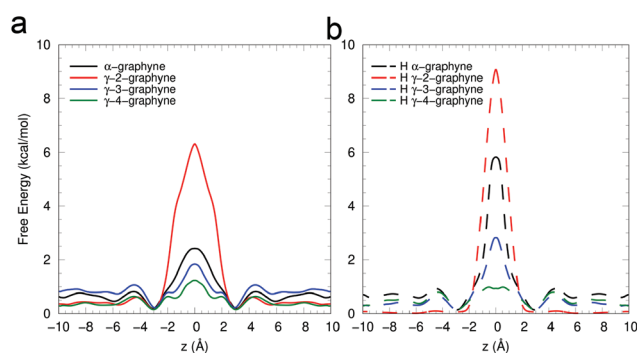


Fig. 7 Energy barriers. Free energy barriers computed for a water molecule along the pore axis of (a) bare and (b) hydrogenated graphyne membranes.

free energy profile are reflected in the water permeabilities of the membranes. The free energy profiles for water molecules passing through the bare membranes show two minor valleys before the peak in the free energy profile. The minor valleys enable the water molecules to pass through the membranes in a stepping mode, wherein the water molecules first jump to the minor valleys and then pass over the peak. This stepping mode enables faster water permeation through these membranes.

Fig. 8a shows the water permeability for different pore types considered in our study: hexagonal (α -graphyne), triangular (γ -{2,3,4}-graphyne), hydrogenated hexagonal (H α -graphyne) and hydrogenated triangular (H γ -{2,3,4}-graphyne). For the triangular and hydrogenated triangular pores, the permeability scales nearly linear with pore area. We can observe that hexagonal pores have a higher water permeation per unit pore area compared to triangular and hydrogenated pores. The water flux through hydrogenated membranes does not drop in proportion to its accessible pore area. A contributing factor is that the hydrogen terminations in H γ -2-graphyne bend outwards to the permeate side, increasing the accessible pore area for these membranes. Water flux is a function of velocity (U) of water through the pore, density (ρ) of water inside the pore and the area of the pore (A). The salt rejection efficiency decreases as the pore area is increased and this leaves ρ and U as the available control parameters to maximize the flux through the pores. To investigate why the hexagonal pores have a higher water flux per unit pore area, we compute U and ρ through the various membranes. Here, the density of water molecules in the pore is calculated by counting the number of water molecules within a distance of 1 \AA across the pore in the direction of the water flow and U was obtained by averaging the velocities of these water molecules over the production run. Results are illustrated in Fig. 8b and c, showing that hexagonal pores have a higher density as well as velocity through them, explaining the higher water flux per unit pore area through them.

To investigate the reason for the higher density and velocity through hexagonal pores, we examine the oxygen density maps of water passing through the pore. We can observe from Fig. 9a and b that hexagonal pores in α -graphyne have a single circular water channel, while triangular pores in γ -3-graphyne have three distinct water channels. The entropic barriers arising from three closely-spaced separate channels give rise to the lower water velocity through the pores. Even though there are distinct water channels, only one water molecule is present within the triangular pore at any given instant as shown in Fig. 9d and this is also indicated by the narrowing of the water channel towards the center of the triangular pore as shown in Fig. 9b. This explains the lower density of water molecules in the membrane. Hexagonal pores have a single channel with water molecules passing through one at a time. The circular cross-section of water flux through hexagonal nanopores gives rise to an hour-glass shaped channeling, which explains the higher flux. Previous studies have shown that canonical nanopores have higher fluxes and permeation rates.^{55–57} Solid-state

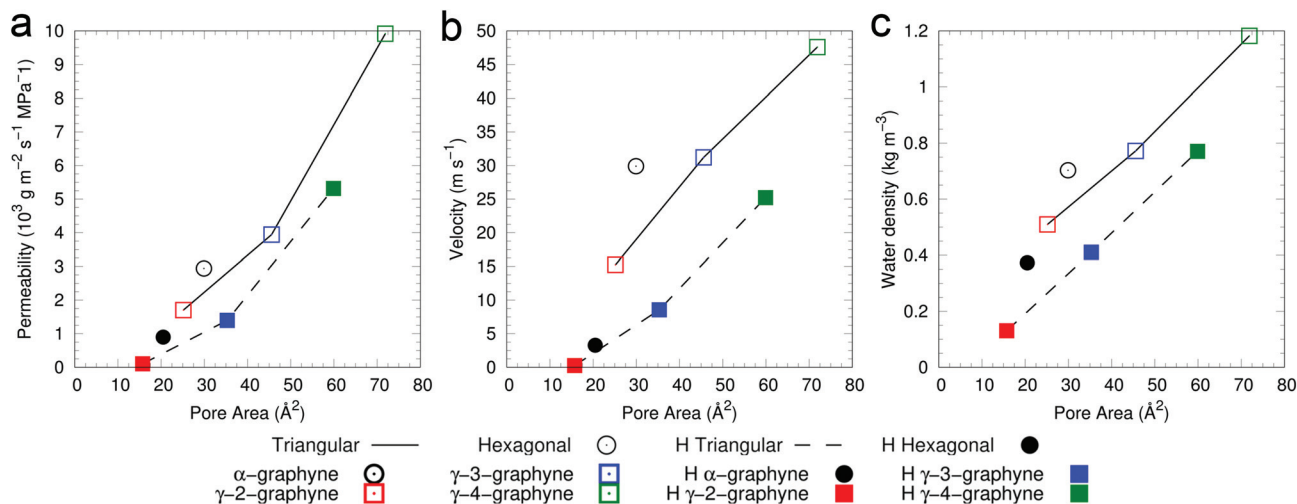


Fig. 8 Effect of pore geometry and pore functionalization on permeability and pore flux. (a) Water permeability and (b, c) Water velocity and density in the pore as a function of pore size for bare and hydrogenated graphyne membranes at 1 GPa.

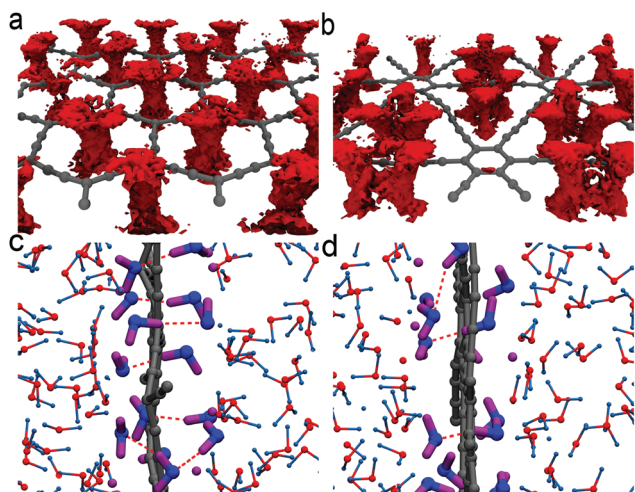


Fig. 9 Water flow across hexagonal and triangular pores. Oxygen density maps (red) inside (a) hexagonal (α -graphyne) and (b) triangular (γ -3-graphyne) pores. Snapshots from MD simulation showing water passing through (c) hexagonal (α -graphyne) and (d) triangular (γ -3-graphyne) pores. The water molecules within 2 Å on either side of the membrane are shown with blue O and purple H atoms. We can observe that in spite of three distinct water channels being present in γ -3-graphyne, only one water molecule is present at a time within the pore.

nanopores have also been tailored with conical shaped water flows to enhance DNA and solute transport.^{58,59} Tailoring the nanopores in 2D membranes to have a hexagonal shape is a pragmatic approach to enhance water flux through nanoporous membranes.

3.2. Upscale analysis of RO desalination

The graphyne membranes considered in this study exhibit water permeabilities that are significantly larger than conventional thin-film composite (TFC) RO membranes.⁵⁴ With rele-

vance to practical applications, it is therefore of interest to evaluate how this increase in membrane permeability affects the energy consumption, specific membrane area and number of pressure vessels employed in an RO plant. To this end, we perform upscale analysis by implementing a 1D numerical model of the mass transport and fluid dynamics of an RO system. In an RO system, feed water enters pressure vessels containing several cylindrical membrane elements, which are connected in series. The feed water travels parallel to the membrane surface and water selectively permeates radially through the membrane. A schematic of a cross-flow RO system is shown in Fig. 10a.

The 1D model of the cross-flow RO system employed in this study follows the derivation of Cohen-Tanugi *et al.*⁵⁴ and is summarized in the following. In this model, results from the MD simulation are used to obtain desalination characteristics for graphyne membranes under consideration. The input parameters are the inlet flow rate (Q_{in}), inlet pressure (P_{in}), inlet bulk salinity ($C_{b,in}$) and the water permeability of the membrane (A_m), which is obtained through MD calculations.

There are two primary quantities that dictate the desalination characteristics, namely pressure and cumulative recovery, which are coupled through a system of ordinary differential equations. The flow through an RO system is modeled as an annular flow problem and thus, the pressure drop is expressed as a function of the flow rate. The key variables and symbols employed in the model are listed in Table 2. The osmotic pressure influences the permeate flux and flow rate through the system, thus coupling the two quantities. The pressure drop can be expressed as

$$\frac{dP}{dz} = -P'_{loss}(z) \quad (2)$$

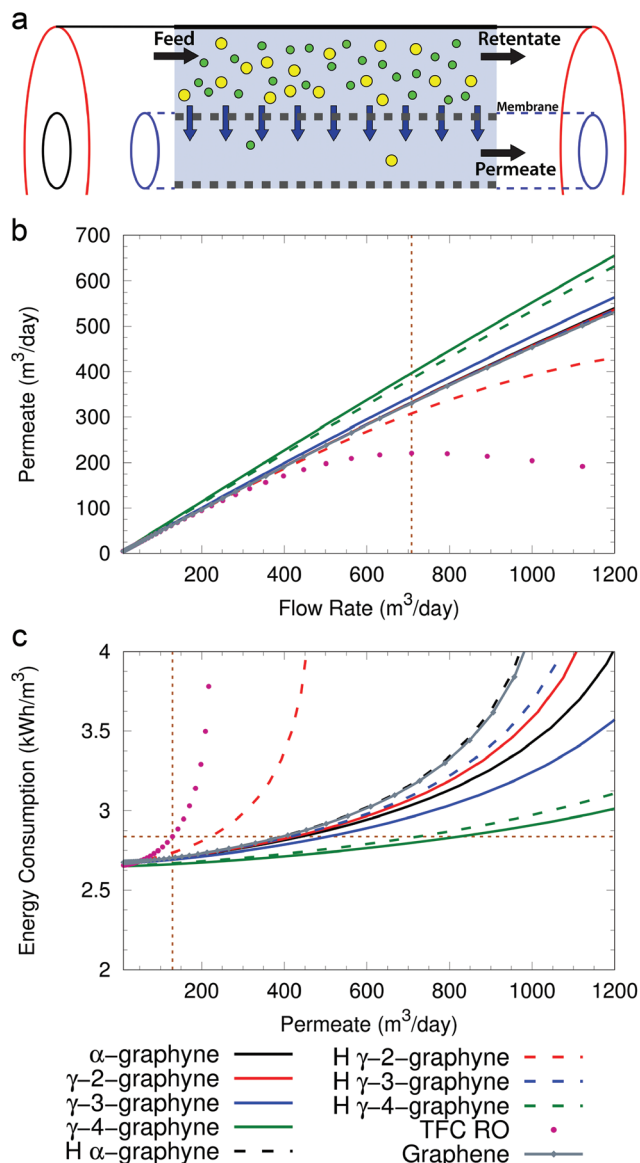


Fig. 10 Upscale analysis of RO system. (a) Schematic representation of cross-flow RO. Permeate recovery and energy consumption. (b) Permeate produced vs. feed flow rate. (c) Specific energy consumption vs. permeate produced.

where P_{loss} represents the pressure loss across the RO vessel and is obtained using the correlation presented in Li *et al.*⁶⁰ for a particular cross-flow RO system, and is determined by the Reynolds number Re , accounting for the effect of viscosity. The second quantity of interest is the cumulative recovery ϕ , given by

$$\frac{d\phi}{dz} = \frac{W}{Q_{\text{in}}} J(z), \quad (3)$$

where W represents the cross-section width and J denotes the permeate flux. In the absence of salt and hence, reverse osmosis, the permeate flux is directly proportional to the permeability of the membrane. However, the presence of salt

Table 2 List of key variables and symbols

Symbol	Quantity	Units
A_m	Water permeability	$L (m^2 h \text{ bar})^{-1}$
c_b	Bulk salinity at position z	ppm
E	Specific power consumption Per unit of permeate	kWh m^{-3}
J	Permeate flux at position z	m s^{-1}
k	Mass transfer coefficient	m s^{-1}
P_{in}	Inlet pressure	Bar
P_{loss}	Pressure lost up to position z	Bar
Q_{in}	Feed flowrate	$\text{m}^3 \text{ day}^{-1}$
\mathcal{R}	Universal gas constant	$\text{J}(\text{K mol})^{-1}$
R_0	Salt rejection rate	%
T	Temperature	K
W	Effective cross-section width	m
ξ	Pressure recovery efficiency	%
η	Pump efficiency	%
$\phi(z)$	Cumulative recovery up to position z	%

exerts an osmotic pressure and the permeate flux in such situations is given by the Van't Hoff equation⁶¹ as

$$J = A_m P - kW \left(\frac{2c_b A_m \mathcal{R} R_0 T}{k} \exp \left\{ \frac{A_m P}{k} \right\} \right), \quad (4)$$

where k represents the mass transfer coefficient and is given by a correlation⁶⁰ based on the Sherwood number, which varies inversely with the diffusivity. c_b is the salinity, or in other words, the salt concentration at the particular location, R_0 is the salt rejection rate, which is evaluated through MD simulations and \mathcal{R} denotes the universal gas constant. In addition, $\mathcal{W}(\xi)$ represents the Lambert W -function with argument ξ and is given by the principal solution of q in the equation $\xi = qe^q$. By solving eqn (3), the flow rate can be written as

$$Q = Q_{\text{in}}(1 - \phi). \quad (5)$$

Since the amount of salt is conserved in the cross-flow system, it follows that

$$c_b = \frac{c_{b,\text{in}}}{1 - \phi}. \quad (6)$$

Eqn (2)–(6) close the system and the relevant quantities can be obtained as a function of axial position z . Two important quantities which are used to evaluate the performance of an RO system are recovery ratio and energy consumption. The recovery ratio is given by $\phi(L)$, where L is the effective length of the membrane and corresponds to the fraction of water recovered from the solution. The energy consumption per unit volume of the permeate⁶² depends on whether a pressure recovery device is used, and can be written as:

$$E = \frac{1 P_{\text{in}} - \zeta(1 - \phi(L))(P_{\text{in}} - P(L))}{\eta \phi(L)}, \quad (7)$$

where η represents the pump efficiency and ζ stands for the pressure recovery device efficiency.

The reference conditions used in this model are listed in Table 3. Additional information on the model setup and

Table 3 Reference parameters for seawater RO system used in this work. Transport properties of water at standard conditions are considered

Reference parameter	SWRO
Bulk feed salinity $C_{b,in}$ [ppm]	42 000
Inlet pressure P_{in} [bar]	70
Dynamic viscosity μ [Pa s]	8.90×10^{-4}
Diffusion coefficient D [$m^2 s^{-1}$]	1.13×10^{-9}
Pressure recovery efficiency ζ	97.0%
Pump efficiency η	75.0%

model parameters is provided as ESI.† Fig. 10b shows the permeate produced per pressure vessel as a function of flow rate for various graphyne membranes considered in our study. The corresponding data for commercial TFC RO and nanoporous graphene is also shown for comparison. It is interesting to note that the two to three orders of magnitude difference in water permeability between TFC RO and graphyne membranes, observed from MD calculations (see Fig. 4), does not directly translate to the permeate production obtained from the 1D cross-flow RO model. This shows the need for an 1D upscaling model to evaluate the improvement in performance of an RO system, given a certain gain in membrane permeability deduced from MD calculations. All of the graphyne membranes exhibit better permeate recovery than TFC RO membranes and, except for H γ -2-graphyne membranes, the remaining graphyne membranes exhibit larger permeate recovery than nanoporous graphene membranes.

To quantify the performance, we compare the permeate produced at the flow rate corresponding to the peak-permeate production of TFC RO membrane ($710 m^3 day^{-1}$, dashed line in Fig. 10b). At this specific flow rate, graphyne membranes produce 60% to 80% more permeate than TFC membranes and up to 20% more permeate as compared to nanoporous graphene membranes.

In addition to permeate production, specific energy consumption has to be considered while evaluating membrane performance for desalination. The energy consumed per unit volume of permeate as a function of permeate production is shown in Fig. 10c. From this figure we can observe that functionalization affects both permeate recovery and energy consumption of an RO system and has to be accounted for while considering the potential of graphyne membranes for desalination. Fig. 10c shows the trade-off between energy savings and pressure vessel savings from graphyne membranes. To achieve a target output, the RO plant can choose to save energy by operating more pressure vessels at a lower feed flow-rate or save installation costs by operating fewer pressure vessels at a higher feed flow-rate. For instance, a targeted permeate production rate of $150 m^3 day^{-1}$ (dashed lines in Fig. 10c), corresponds to energy savings up to 6% or up to 6 times fewer pressure vessels while employing graphyne membranes as compared to TFC membranes. The energy savings are limited due to the fact that current RO plants operate near the lowest required inlet pressure to extract permeate water

from seawater at the expense of low permeate production per vessel.⁶³ However, the higher permeability of graphyne membranes shows encouraging trends with regards to capital costs, provided graphyne membranes can be manufactured at costs comparable to current TFC membranes. The savings can be significant, since pressure vessels and associated membranes and piping attribute to approximately 20% of the capital costs of a RO plant, which ranges in the hundreds of millions of US dollars. Therefore, even though the energy savings are limited, nanoporous graphyne membranes can provide significant savings by reducing the number of pressure vessels, which is also attractive for space-constrained desalination applications.

4. Conclusions

In conclusion, our MD simulations indicate that nanoporous graphyne membranes reject salt ions while allowing water permeabilities up to three orders of magnitude higher than existing seawater RO membranes and up to ten times that of nanoporous graphene and MoS_2 membranes. Graphyne offers the advantage of a uniform pore distribution unlike nanoporous graphene, and exhibits higher water permeabilities while still rejecting salt ions. γ -{2,3}-graphyne, H γ -3-graphyne, α -graphyne and H α -graphyne membranes are able to reject the majority (>90%) of the salt ions while permitting higher water fluxes. Therefore, they appear to be attractive candidates for desalination systems among the membranes considered in our study. Our simulations indicate that both water flux and salt rejection are sensitive to accessible pore area, pore geometry and chemical functionalization. We observe that the conical water flow in the hexagonal pores (α -graphyne) allows for a high water flux per unit accessible area compared to triangular pores.

Upscale analysis of RO plants employing graphyne membranes shows that relative to today's baseline (TFC RO), ultra permeable membranes could produce more permeate and consume less energy. However, the orders of magnitude difference in water permeability observed in MD simulations does not translate to the macroscopic RO system. Graphyne membranes still offer up to six times higher permeate recovery and ~6% lower energy consumption for a permeate production rate at currently accessible operating conditions of $150 m^3 day^{-1}$; substantially higher energy savings and permeate recovery can be achieved if higher feed-flow rates can be realized. For instance, we can observe from Fig. 10(c) that, at permeate production rate of $200 m^3 day^{-1}$, the best possible energy savings increases to 13%. The higher permeability of graphyne membranes could significantly reduce the capital costs of a RO plant without affecting permeate recovery or energy consumption. However, the energy savings are limited because the current RO plants operate close to the minimum pressure required to extract permeate water from seawater. An upscaling model in conjunction with MD simulations is essential to evaluate the potential of nanoporous membranes for water desalination.

Pore functionalization can also be employed to selectively filter differently charged ions by choosing specific functional groups to decorate the pores. For instance, we observe that hydrogenated pores in γ -4-graphyne membranes can selectively permeate negatively charged ions (Cl^-) while rejecting positively charged salt ions (Na^+ and K^+). Conversely oxygenated γ -4-graphyne membranes can be expected to selectively permeate positively charged ions (Na^+ and K^+) while repelling negatively charged Cl^- ions. These functionalized γ -4-graphyne membranes have potential application as ion exchange membranes in membrane capacitive deionization.

Conflicts of interest

The authors declare no competing financial interest.

Acknowledgements

Financial support through the Army Research Laboratory with award number W911NF-16-2-0170 is gratefully acknowledged. ACTvD acknowledges funding from the Fluid Interface Reactions, Structures and Transport (FIRST) Center, an Energy Frontier Research Center funded by the U.S. Department of Energy, Office of Science, Office of Basic Energy Sciences. This work was partially inspired by the FIRST-related simulations and experiments on the behavior of water around functionalized graphene defects. MI acknowledges support through the DFG Mercator Fellowship SPP1980 "SpraySyn: Nanopartikelsynthese in Sprayflammen".

References

- M. Elimelech and W. A. Phillip, *Science*, 2011, **333**, 712–717.
- M. A. Shannon, P. W. Bohn, M. Elimelech, J. G. Georgiadis, B. J. Marinas and A. M. Mayes, *Nature*, 2008, **452**, 301–310.
- A. D. Khawaji, I. K. Kutubkhanah and J.-M. Wie, *Desalination*, 2008, **221**, 47–69.
- A. Subramani and J. G. Jacangelo, *Water Res.*, 2015, **75**, 164–187.
- M. M. Pendergast and E. M. V. Hoek, *Energy Environ. Sci.*, 2011, **4**, 1946–1971.
- D. Cohen-Tanugi and J. C. Grossman, *Nano Lett.*, 2012, **12**, 3602–3608.
- C. Zhu, H. Li, X. C. Zeng, E. G. Wang and S. Meng, *Sci. Rep.*, 2013, **3**, 3163.
- L. Wang, M. S. H. Boutilier, P. R. Kidambi, D. Jang, N. G. Hadjiconstantinou and R. Karnik, *Nat. Nanotechnol.*, 2017, **12**, 509–522.
- L. X. Li, J. H. Dong, T. M. Nenoff and R. Lee, *J. Membr. Sci.*, 2004, **243**, 401–404.
- L. Li, N. Liu, B. McPherson and R. Lee, *Desalination*, 2008, **228**, 217–225.
- F. Fornasiero, J. B. In, S. Kim, H. G. Park, Y. Wang, C. P. Grigoropoulos, A. Noy and O. Bakajin, *Langmuir*, 2010, **26**, 14848–14853.
- F. Fornasiero, H. G. Park, J. K. Holt, M. Stadermann, C. P. Grigoropoulos, A. Noy and O. Bakajin, *Proc. Natl. Acad. Sci. U. S. A.*, 2008, **105**, 17250–17255.
- B. J. Hinds, N. Chopra, T. Rantell, R. Andrews, V. Gavalas and L. G. Bachas, *Science*, 2004, **303**, 62–65.
- D. Cohen-Tanugi and J. C. Grossman, *J. Chem. Phys.*, 2014, **141**, 074704.
- S. P. Surwade, S. N. Smirnov, I. V. Vlasiouk, R. R. Unocic, G. M. Veith, S. Dai and S. M. Mahurin, *Nat. Nanotechnol.*, 2015, **10**, 459–464.
- M. Heiranian, A. B. Farimani and N. R. Aluru, *Nat. Commun.*, 2015, **6**, 8616.
- R. H. Baughman, H. Eckhardt and M. Kertesz, *J. Chem. Phys.*, 1987, **87**, 6687–6699.
- U. H. F. Bunz, Y. Rubin and Y. Tobe, *Chem. Soc. Rev.*, 1999, **28**, 107–119.
- F. Diederich, *Nature*, 1994, **369**, 199–207.
- V. R. Coluci, S. F. Braga, S. B. Legoas, D. S. Galvao and R. H. Baughman, *Phys. Rev. B: Condens. Matter Mater. Phys.*, 2003, **68**, 035430.
- A. Hirsch, *Nat. Mater.*, 2010, **9**, 868–871.
- G. Li, Y. Li, H. Liu, Y. Guo, Y. Li and D. Zhu, *Chem. Commun.*, 2010, **46**, 3256–3258.
- Y. Li, L. Xu, H. Liu and Y. Li, *Chem. Soc. Rev.*, 2014, **43**, 2572–2586.
- Z. Jia, Y. Li, Z. Zuo, H. Liu, C. Huang and Y. Li, *Acc. Chem. Res.*, 2017, **50**, 2470–2478.
- S. W. Cranford and M. J. Buehler, *Carbon*, 2011, **49**, 4111–4121.
- W. Wu, W. Guo and X. C. Zeng, *Nanoscale*, 2013, **5**, 9264–9276.
- D. Malko, C. Neiss, F. Vines and A. Goerling, *Phys. Rev. Lett.*, 2012, **108**, 086804.
- S. W. Cranford, D. B. Brommer and M. J. Buehler, *Nanoscale*, 2012, **4**, 7797–7809.
- Y. Yang and X. Xu, *Comput. Mater. Sci.*, 2012, **61**, 83–88.
- J. Kou, X. Zhou, H. Lu, F. Wu and J. Fan, *Nanoscale*, 2014, **6**, 1865–1870.
- G. M. Psfogiannakis and G. E. Froudakis, *J. Phys. Chem. C*, 2012, **116**, 19211–19214.
- R. Longuinhos, E. A. Moujaes, S. S. Alexandre and R. W. Nunes, *Chem. Mater.*, 2014, **26**, 3701–3708.
- J. Kou, X. Zhou, Y. Chen, H. Lu, F. Wu and J. Fan, *J. Chem. Phys.*, 2013, **139**, 064705.
- S. Lin and M. J. Buehler, *Nanoscale*, 2013, **5**, 11801–11807.
- M. Xue, H. Qiu and W. Guo, *Nanotechnology*, 2013, **24**, 1–7.
- A. C. T. van Duin, S. Dasgupta, F. Lorant and W. A. Goddard III, *J. Phys. Chem. A*, 2001, **105**, 9396–9409.
- M. C. Hatzell, M. Raju, V. J. Watson, A. G. Stack, A. C. T. van Duin and B. E. Logan, *Environ. Sci. Technol.*, 2014, **48**, 14041–14048.
- M. Raju, A. C. T. van Duin and K. A. Fichthorn, *Nano Lett.*, 2014, **14**, 1836–1842.

- 39 T. P. Senftle, S. Hong, M. M. Islam, S. B. Kylasa, Y. Zheng, Y. K. Shin, C. Junkermeier, R. Engel-Herbert, M. J. Janik, H. M. Aktulga, T. Verstraelen, A. Grama and A. C. T. van Duin, *npj Comput. Mater.*, 2016, **2**, 1–14.
- 40 O. Rahaman, A. C. T. van Duin, V. S. Bryantsev, J. E. Mueller, S. D. Solares, W. A. Goddard and D. J. Doren, *J. Phys. Chem. A*, 2010, **114**, 3556–3568.
- 41 O. Rahaman, A. C. T. van Duin, W. A. Goddard and D. J. Doren, *J. Phys. Chem. B*, 2011, **115**, 249–261.
- 42 M. Raju, P. Ganesh, P. R. C. Kent and A. C. T. van Duin, *J. Chem. Theory Comput.*, 2015, **11**, 2156–2166.
- 43 K. D. Nielson, A. C. T. van Duin, J. Oxgaard, W.-Q. Deng and W. A. Goddard III, *J. Phys. Chem. A*, 2005, **109**, 493–499.
- 44 X. Huang, H. Yang, W. Liang, M. Raju, M. Terrones, V. H. Crespi, A. C. T. van Duin and S. Zhang, *Appl. Phys. Lett.*, 2013, **103**, 1–4.
- 45 S. G. Srinivasan, A. C. T. van Duin and P. Ganesh, *J. Phys. Chem. A*, 2015, **119**, 571–580.
- 46 S. Plimpton, *J. Comput. Phys.*, 1995, **117**, 1–19.
- 47 R. Mills, *J. Phys. Chem.*, 1973, **77**, 685–688.
- 48 M. Holz, S. R. Heil and A. Sacco, *Phys. Chem. Chem. Phys.*, 2000, **2**, 4740–4742.
- 49 G. M. Torrie and J. P. Valleau, *Chem. Phys. Lett.*, 1974, **28**, 578–581.
- 50 M. Bonomi, D. Branduardi, G. Bussi, C. Camilloni, D. Provasi, P. Raiteri, D. Donadio, F. Marinelli, F. Pietrucci, R. A. Broglia and M. Parrinello, *Comput. Phys. Commun.*, 2009, **180**, 1961–1972.
- 51 A. Grossfield, WHAM: the weighted histogram analysis method, <http://membrane.urmc.rochester.edu/content/wham>.
- 52 C. Fritzmann, J. L  wenberg, T. Wintgens and T. Melin, *Desalination*, 2007, **216**, 1–76.
- 53 G. Guillen and E. M. V. Hoek, *Chem. Eng. J.*, 2009, **149**, 221–231.
- 54 D. Cohen-Tanugi, R. K. McGovern, S. H. Dave, J. H. Lienhard and J. C. Grossman, *Energy Environ. Sci.*, 2014, **7**, 1134–1141.
- 55 S. Gravelle, L. Joly, C. Ybert and L. Bocquet, *J. Chem. Phys.*, 2014, **141**, 1–7.
- 56 S. Gravelle, L. Joly, F. Detcheverry, C. Ybert, C. Cottin-Bizonne and L. Bocquet, *Proc. Natl. Acad. Sci. U. S. A.*, 2013, **110**, 16367–16372.
- 57 L. Bocquet and P. Tabeling, *Lab Chip*, 2014, **14**, 3143–3158.
- 58 C. Dekker, *Nat. Nanotechnol.*, 2007, **2**, 209–215.
- 59 E. A. Heins, Z. S. Siwy, L. A. Baker and C. R. Martin, *Nano Lett.*, 2005, **5**, 1824–1829.
- 60 F. Li, W. Meindersma, A. B. De Haan and T. Reith, *J. Membr. Sci.*, 2002, **208**, 289–302.
- 61 E. M. V. Hoek, A. S. Kim and M. Elimelech, *Environ. Eng. Sci.*, 2002, **19**, 357–372.
- 62 K. H. Mistry, R. K. McGovern, G. P. Thiel, E. K. Summers, S. M. Zubair and J. H. Lienhard, *Entropy*, 2011, **13**, 1829–1864.
- 63 R. K. McGovern and J. H. L. V., *J. Membr. Sci.*, 2016, **520**, 560–565.